Direct numerical simulations of the interaction of temporally evolving circular jets

Tomoaki Watanabe,[1] † Tatsuya Inagaki,[2] Takahiro Mori,[2] Kirari Ishizawa[3] and Koji Nagata[1]

[1]Department of Mechanical Engineering and Science, Kyoto University, Kyoto 615-8540, Japan

[2]Department of Aerospace Engineering, Nagoya University, Nagoya 464-8603, Japan

[3]Undergraduate Department of Mechanical and Aerospace Engineering, Nagoya University, Nagoya 464-8603, Japan

(Received xx; revised xx; accepted xx)

Direct numerical simulations are performed to study turbulence generated by the interaction of multiple temporally evolving circular jets with jet Mach numbers $M_J = 0.6$ and 1.6, and a jet Reynolds number of 3000. The jet interaction produces decaying, nearly homogeneous isotropic turbulence, where the root-mean-squared (rms) fluctuation ratio between the streamwise and transverse velocities is approximately 1.1, consistent with values observed in grid turbulence. In the supersonic case, shock waves are generated and propagate for a long time, even after the turbulent Mach number decreases. A comparison between the two Mach number cases reveals compressibility effects, such as reductions in the velocity derivative skewness magnitude and the non-dimensional energy dissipation rate. For the rms velocity fluctuations, u_{rms}, and the integral scale of the streamwise velocity, L_u, the Batchelor turbulence invariant, $u_{rms}^2 L_u^5$, becomes nearly constant after the turbulence has decayed for a certain time. In contrast, the Saffman turbulence invariant, $u_{rms}^2 L_u^3$, continuously decreases. Furthermore, temporal variations of u_{rms}^2 and L_u follow power laws, with exponents closely matching the theoretical values for Batchelor turbulence. The three-dimensional energy spectrum $E(k)$, where k is the wavenumber, exhibits $E(k) \sim k^4$ for small wavenumbers. This behaviour is consistently observed for both Mach number cases, indicating that the modulation of small-scale turbulence by compressibility effects does not affect the decay characteristics of large scales. These results demonstrate that jet interaction generates Batchelor turbulence, providing a new direction for experimental investigations into Batchelor turbulence using jet arrays.

1. Introduction

A complex turbulent flow resulting from the interaction of jets has significant engineering applications, including cooling systems (Geers *et al.* 2006; Caliskan *et al.* 2014), combus-

† Email address for correspondence: watanabe.tomoaki.8x@kyoto-u.ac.jp

Abstract must not spill onto p.2

tors (Burr & Ken 2019; Yang *et al.* 2021), and air conditioning systems (Medaouar *et al.* 2019). In environmental flows, similar interactions are observed in plumes from stacked chimneys (Bornoff & Mokhtarzadeh-Dehghan 2001) and exhausts from air-cooled condenser arrays (Liu *et al.* 2009). High-speed jet interactions are also relevant to supersonic aircraft, where jet-induced noise is a critical factor in design and development (Raman & Taghavi 1996). These practical challenges have motivated extensive research on jet interactions in various configurations, as summarised in the literature review by Boussoufi *et al.* (2017).

The simplest jet interaction occurs in confluent jets issued from two identical nozzles. This flow configuration, involving both planar and circular jets, has been extensively studied (Miller & Comings 1960; Lin & Sheu 1990; Anderson & Spall 2001; Manohar *et al.* 2004; Meslem *et al.* 2010; Hao *et al.* 2021). These studies have identified distinct regimes in jet interaction, including converging, merging and combined regions, highlighting the flow evolution during the interaction. Initially, the separated jets converge toward the centreline between the two jets. For planar jets, a recirculation zone forms between the jets in the converging region. Strong jet interaction occurs in the merging region, where the centreline velocity between the jets increases. Further downstream lies the combined region, where the centreline mean velocity decays similarly to a single jet. Multiple confluent jets issued from nozzle arrays into free space have also been studied, though less extensively than dual jets (Yimer *et al.* 1996; Meslem *et al.* 2010; Ghahremanian *et al.* 2014; Svensson *et al.* 2016). These studies reveal entrainment of surrounding fluid into the freely evolving multiple jets, which contributes to the decay of the mean streamwise velocity. The nozzle shape and configuration influence flow development in the near field but have minimal impact on the far field, where the combined jet exhibits characteristics similar to a single jet. Research on supersonic jet interactions has primarily focused on jet noise (Coltrin *et al.* 2013, 2014). Additionally, numerous studies have investigated impinging multiple jets due to their applications in heating and cooling devices (Thielen *et al.* 2003; Geers *et al.* 2005).

Confined multiple confluent jets have also been studied extensively (Teunissen 1975; Tatsumi *et al.* 2010; Tan *et al.* 2023; Mori *et al.* 2024). When a large number of nozzles are arranged in a square array, jet interaction leads to the formation of decaying homogeneous isotropic turbulence (HIT). A similar formation of decaying HIT has been reported for unconfined square jet arrays in the early stage of the combined region, where the flow near the centreline becomes nearly homogeneous in the cross-streamwise plane (Ghahremanian *et al.* 2014). As detailed below, the behaviour of decaying HIT strongly depends on the turbulence generation mechanism. Accordingly, some previous studies have conducted experiments with multiple confluent jets to examine HIT (Tan *et al.* 2023; Mori *et al.* 2024). The aforementioned studies primarily focus on continuous jets. However, the formation of HIT has also been observed in studies of unsteady jet interactions, such as pulse-operated jets (Bellani & Variano 2014; Carter *et al.* 2016; Pérez-Alvarado *et al.* 2016) and synthetic jets (Hwang & Eaton 2004; Variano *et al.* 2004; Yamamoto *et al.* 2022*b*). Some of these studies explore the collision of multiple jets from several arrays. The turbulence generation mechanisms differ between continuous and unsteady jets: the former is associated with turbulent kinetic energy production due to mean shear, while the latter is influenced by temporal variations in jet velocity.

HIT is one of the most fundamental issues in turbulence research (Davidson 2004). The assumption of statistical homogeneity and isotropy simplifies the problem, facilitating the development of statistical theories. Most theories have been formulated for the statistics of small-scale motions, which are believed to exhibit some universal properties. Fewer theories target large scales, despite their dominant role in various turbulent phenomena, such as turbulent mixing. Notable exceptions include the theories of Saffman and Batchelor turbulence, which describe HIT with three-dimensional energy spectra $E(k) = Lk^2/4\pi^2$ and

$Ik^4/24\pi^2$, respectively, with a small wavenumber k (Saffman 1967; Batchelor & Proudman 1956; Davidson 2004). Saffman turbulence is characterised by linear momentum, whose conservation results in the Saffman integral L being constant. In scenarios where $L = 0$, the Loitsyansky integral I related to angular momentum remains approximately constant when long-range correlations are negligible, leading to the Batchelor theory. These invariants constrain root-mean-squared (rms) velocity fluctuations U and integral length scale L during decay, where U^2L^3 = Const. for Saffman turbulence and U^2L^5 = Const. for Batchelor turbulence, provided that the large scales evolve in a self-similar manner. The variation of the non-dimensional dissipation rate $C_\varepsilon = \varepsilon/(U^3/L)$ in decaying HIT is often described by $C_\varepsilon \sim (t - t_0)^{n_C}$, where ε is the dissipation rate of turbulent kinetic energy (TKE) per unit mass and t_0 is a virtual origin of decay (Krogstad & Davidson 2010). A constant C_ε at high Reynolds numbers implies $n_C = 0$. Non-equilibrium dissipation scaling or low Reynolds number effects result in $n_C > 0$ (Meldi & Sagaut 2013; Valente & Vassilicos 2014; Kitamura *et al.* 2014). The evolution of U^2 and L can be expressed as

$$U^2 \sim (t - t_0)^{-10(1+n_C)/7}, \quad L \sim (t - t_0)^{2(1+n_C)/7} \quad \text{for Batchelor turbulence,} \tag{1.1}$$

$$U^2 \sim (t - t_0)^{-6(1+n_C)/5}, \quad L \sim (t - t_0)^{2(1+n_C)/5} \quad \text{for Saffman turbulence,} \tag{1.2}$$

where (1.1) is referred to as the Kolmogorov decay law (Kolmogorov 1941; Krogstad & Davidson 2010).

Experiments of HIT have been conducted to validate theories and models of turbulence, including Saffman and Batchelor theories. Grid turbulence is often studied as an approximation to HIT, employing various grids designed to generate HIT with desired properties. These grids vary in their geometries, including shapes and configurations of grid bars. Some of grid turbulence experiments demonstrate that the decay law follows that of Saffman turbulence, for various types of grid (Praud *et al.* 2005; Krogstad & Davidson 2010, 2011; Kitamura *et al.* 2014; Sinhuber *et al.* 2015; Watanabe *et al.* 2022). On the other hand, the observation of the Kolmogorov decay law has been limited to an early study of grid turbulence at extremely low Reynolds numbers (Batchelor & Townsend 1948). This evidence is also considered weak because it relies solely on the decay of U, rather than on the invariance of U^2L^5 or the variations of both U and L. Although the theories discussed above predict the decay laws for turbulence with $E(k) \sim k^2$ or $E(k) \sim k^4$, they do not explain under what conditions turbulence with such spectra is generated, such as how to produce turbulence with or without net linear momentum. Whether the decay of HIT follows the laws of Saffman turbulence, Batchelor turbulence or neither is expected to depend on the method of turbulence generation. Therefore, it is essential to examine decaying HIT generated by various methods and compare the results with the theoretical decay laws. It is important to note that numerical studies on Saffman and Batchelor turbulence typically examine the decay of isotropic turbulence, where the spectrum is artificially initialised to follow $E(k) \sim k^2$ or $E(k) \sim k^4$. The formation of Saffman or Batchelor turbulence relates to the transition from laminar to turbulent flow, such as turbulence generated by grids. Such studies are primarily limited to grid turbulence, as discussed earlier. While multiple jet interactions are known to generate HIT, their relevance to the decay laws of Saffman and Batchelor turbulence has been scarcely explored.

The present study investigates the decay of nearly HIT generated by multiple jet interactions. Direct numerical simulations (DNS) are performed for temporally evolving circular jets. Temporal shear flows are commonly considered in fundamental turbulence studies as approximations of spatial flows, such as jets (da Silva & Pereira 2008; Sadeghi *et al.* 2018; Hayashi *et al.* 2021*a*), wakes (Diamessis *et al.* 2011; Watanabe *et al.* 2016*a*; Zecchetto & da Silva 2021), mixing layers (Gampert *et al.* 2014; Watanabe *et al.* 2016*b*; Blakeley *et al.* 2022) and boundary layers (Kozul *et al.* 2016; Watanabe *et al.*

2018; Zhang *et al.* 2018). Temporal simulations employ periodic boundary conditions in the streamwise direction, allowing the flow to evolve over time rather than spatially. Previous studies have demonstrated that the turbulence generation process due to mean shear is similar for both temporal and spatial flows. Using this approach, DNS of grid turbulence has been conducted as a temporal wake of a grid, showing good agreement with spatially evolving grid turbulence observed in experiments (Watanabe & Nagata 2018; Watanabe *et al.* 2022). The present study adopts the same methodology for jet interactions. Temporal simulations are computationally less expensive than spatial simulations, enabling the use of a very large computational domain where turbulence decay is unaffected by boundary conditions. Additionally, periodic boundary conditions in the streamwise direction allow direct evaluation of the three-dimensional energy spectrum, facilitating comparison with $E(k) \sim k^2$ and $E(k) \sim k^4$. Consequently, this study focuses on temporally evolving jets. DNS is conducted for both subsonic and supersonic jets. This DNS demonstrates that turbulence arising from jet interactions behaves similarly to Batchelor turbulence. In the supersonic case, fluid compressibility potentially affects turbulence decay, with such effects prominent in both transitional and decay regimes. A supersonic jet generates shock waves during the initial transitional regime. These waves propagate into the far field, influencing small-scale flow features, such as velocity gradient statistics (Yamamoto *et al.* 2022*a*). The present DNS also aims to explore how the modulation of small scales by these waves affects the large-scale flow features described in the theories of Batchelor and Saffman turbulence.

Previous DNS studies on Batchelor and Saffman turbulence have primarily focused on validating the respective theories (Ishida *et al.* 2006; Anas *et al.* 2020; Davidson *et al.* 2012). These studies typically employ DNS with initial conditions specifically designed so that the initial energy spectrum $E(k)$ follows k^4 or k^2. The decay of turbulence with $E(k) \sim k^4$ or k^2 is then compared against the theoretical predictions. Such investigations require the turbulence to be incompressible, homogeneous and strictly isotropic, as assumed in the theories. In contrast, the present study aims to examine the decay properties of turbulence generated by jet interaction. The present DNS does not impose a spectral shape of $E(k) \sim k^4$ or k^2 in the initial condition. Instead, these spectral shapes may emerge during the turbulent transition from the jet interaction, as the initial condition is laminar. In this sense, the present DNS differs from earlier studies of Batchelor and Saffman turbulence. It provides insights into how Batchelor or Saffman turbulence can develop from a laminar state, rather than focusing solely on whether the theoretical decay laws of Batchelor and Saffman turbulence are recovered in turbulence with pre-imposed spectral shapes of $E(k) \sim k^4$ or k^2.

The paper is organised as follows. Section 2 describes the numerical details of temporally evolving jets. Section 3 presents the DNS results, including the formation of nearly HIT from the jet interaction, compressiblity effects on small-scale characteristics of turbulence and decay behaviour. Finaly, the findings from the DNS are summerised in § 4.

2. Direct numerical simulations for the interaction of temporally evolving jets

2.1. *Temporally evolving jets*

DNS is utilised to study temporally-evolving multiple jets, applying methodologies of temporal jets and grid turbulence (da Silva & Pereira 2008; Sadeghi *et al.* 2018; Watanabe & Nagata 2018; Watanabe *et al.* 2022). Figure 1 illustrates a schematic of the initial field used in the present DNS. The number of jets shown is illustrative and does not correspond to the actual number in the simulations. Temporal jets, with an initial diameter of D, are positioned at an equal spacing of S in the y- and z-directions. The initial velocity profile of each jet matches that of temporal round jets studied previously (Pineau & Bogey

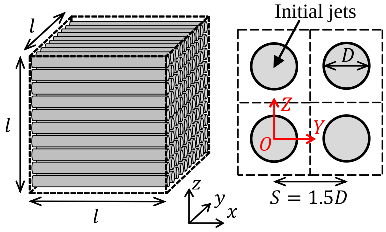

Figure 1: A schematic of the initial field for the DNS of temporally evolving jet interactions. The initial jet regions are depicted in grey. The number of jets shown is illustrative and does not match the actual value of 40. The figure also displays the coordinate system (Y, Z), which is used for statistical evaluations.

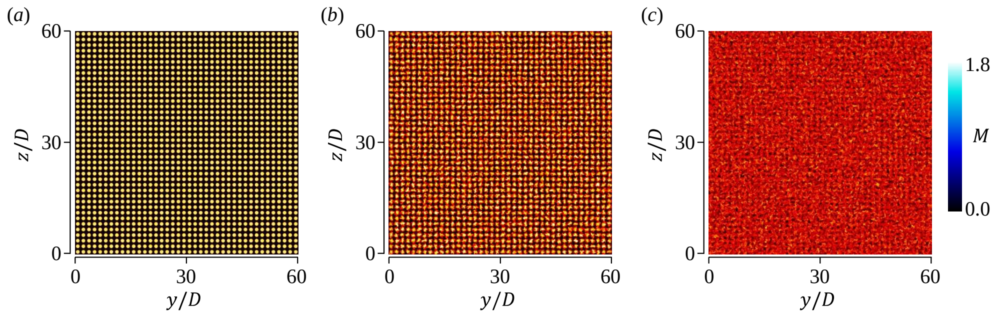

Figure 2: Local Mach number $M = \sqrt{u^2 + v^2 + w^2}/a$ on a y–z plane for M16 at (*a*) $t/T_J = 0$, (*b*) $t/T_J = 8$ and (*c*) $t/T_J = 13$, where a is the local speed of sound.

2020; Takahashi *et al.* 2023), with its mathematical expression provided below. The temporal jets evolve over time within a triply periodic domain, becoming turbulent due to instabilities associated with their mean velocity profiles. Interactions among the jets result in the formation of nearly HIT. As all jets are statistically equivalent, statistics are evaluated by spatial averages in the streamwise direction and ensemble averages across all jets, expressed as functions of the local jet coordinate (Y, Z) centred at each jet, as shown in figure 1. The average is denoted by $\langle f \rangle$, fluctuations by $f' = f - \langle f \rangle$, and the root-mean-square (rms) value by $f_{rms} = \langle f'^2 \rangle^{1/2}$. Two simulations are performed, one for subsonic and the other for supersonic jet velocities.

The governing equations are the compressible Navier–Stokes equations and the equation of state for an ideal gas, expressed as follows:

$$\frac{\partial \rho}{\partial t} + \frac{\partial \rho u_j}{\partial x_j} = 0, \tag{2.1}$$

$$\frac{\partial \rho u_i}{\partial t} + \frac{\partial \rho u_i u_j}{\partial x_j} = -\frac{\partial P}{\partial x_i} + \frac{\partial \tau_{ij}}{\partial x_j}, \tag{2.2}$$

$$c_v \frac{\partial \rho T}{\partial t} + c_v \frac{\partial \rho T u_j}{\partial x_j} = -P \frac{\partial u_j}{\partial x_j} + \frac{\partial}{\partial x_j}\left(\kappa \frac{\partial T}{\partial x_j}\right) + \tau_{ij} \frac{\partial u_i}{\partial x_j}, \tag{2.3}$$

$$P = \rho R T. \tag{2.4}$$

The viscous stress tensor τ_{ij} is written as:

$$\tau_{ij} = \mu \left(\frac{\partial u_i}{\partial x_j} + \frac{\partial u_j}{\partial x_i} - \frac{2}{3}\delta_{ij}\frac{\partial u_k}{\partial x_k} \right). \tag{2.5}$$

Here, ρ is the density, u_i is the velocity, P is the pressure, T is the temperature, μ is the viscosity, κ is the thermal conductivity and δ_{ij} is the Kronecker delta. The simulations assume air as the working gas, characterised by a gas constant $R = 287$ J/(kg·K), a specific heat ratio $\gamma = 1.4$ and a Prandtl number $Pr = 0.71$. The viscosity coefficient μ is determined using Sutherland's law.

The mean streamwise velocity of each jet, centered at coordinates (y_C, z_C), is defined as: $\langle u \rangle = 0.5U_J + 0.5U_J \tanh[(D - 2|r|)/4\theta_J]$ with $r(y,z) = \sqrt{(y-y_C)^2 + (z-z_C)^2}$, where U_J is the initial jet velocity, D is the diameter and $\theta_J = 0.03D$ represents the shear layer thickness at the jet edge. Hereafter, the subscript J refers to quantities related to the initial jet. The initial mean velocity is uniform in the streamwise direction. This methodology follows the DNS studies of a single temporal jet (da Silva & Pereira 2008). The combined mean velocity profiles of all jets establish the initial mean velocity field. Weak spatially-correlated random noise with a scale of $0.25D$ and rms values of $0.02U_J$ is superimposed on the mean velocity inside the jets to trigger the shear instability (Nagata *et al.* 2018). The rms value is close to those measured at a jet nozzle in several studies (Ghahremanian *et al.* 2014; Watanabe *et al.* 2014). The initial conditions are set with constant temperature $T = 300$ K and pressure $P = 1.013 \times 10^5$ Pa. The flow is characterised by the jet Reynolds number and Mach number, given as $Re_J = \rho_J U_J D/\mu_J$ and $M_J = U_J/a_J$, where $a_J = \sqrt{\gamma R T_J}$ is the speed of sound in the jet.

2.2. *Numerical methods and parameters*

The simulations are conducted for $M_J = 0.6$ and 1.6 with $Re_J = 3000$, referred to as M06 and M16, respectively. The corresponding convective Mach numbers, defined as $M_C = M_J/2$, are 0.3 and 0.8, respectively. For $M_C = 0.3$, the initial shear instability is expected to be minimally affected by compressibility, while for $M_C = 0.8$, the transition to turbulence is delayed, as demonstrated below (Freund *et al.* 2000; Pantano & Sarkar 2002). The normalised jet spacing S/D is set to 1.5, and the number of jets, N_J^2, is 40^2. We have confirmed through additional DNS with a smaller jet number that the formaton of nearly HIT are minimally affected by S/D between 1.125 and 2.0, which mainly influences the time required for turbulence development. Figure 2(a) shows the initial field with the local Mach number distribution.

The governing equations are solved with an inhouse DNS code based on finite difference schemes, whose details can be found in Yamamoto *et al.* (2022a). Spatial discretization is achieved through a hybrid scheme that combines a sixth-order central difference scheme and a fifth-order weighted essentially non-oscillatory scheme used together with the advection upstream splitting method (Jiang & Shu 1996; San & Kara 2015). The former is applied to smooth regions, while the latter is used for highly compressive regions, defined as $\Theta < -5\Theta_{rms}$, where Θ_{rms} represents the rms fluctuations of the dilatation $\Theta = \partial u_j/\partial x_j$. The equations are temporally integrated using a third-order total-variation-diminishing Runge–Kutta scheme (Gottlieb & Shu 1998).

The computational domain is cubic with a side length of $l = N_J S$. The reference timescale of the jet is defined as $T_J = D/U_J$. Here, the present study defines the timescale using the jet diameter D rather than the spacing S, as the development of turbulence through jet interaction is characterised by D (Tan *et al.* 2023). Time is advanced until $t = 5000T_J$. Statistics are evaluated as functions of time and (Y, Z) with streamwise averages and ensemble averages across different jets. The time step is set with a constant Courant–Friedrichs–Lewy

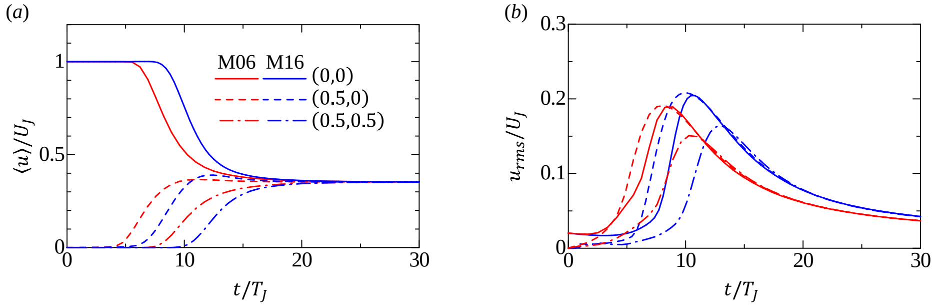

Figure 3: Temporal variations of (*a*) mean streamwise velocity $\langle u \rangle$ and (*b*) rms fluctuations of streamwise velocity u_{rms} at $(Y/S, Z/S) = (0, 0)$, $(0.5, 0)$ and $(0.5, 0.5)$ for M06 and M16.

number of 0.3. As the Kolmogorov scale increases over time, the grid resolution is adjusted accordingly. The numbers of grid points for time intervals $0 \leqslant t/T_J \leqslant 40$, $40 \leqslant t/T_J \leqslant 100$, $100 \leqslant t/T_J \leqslant 520$ and $520 \leqslant t/T_J \leqslant 5000$ are denoted by N_1^3, N_2^3, N_3^3 and N_4^3, respectively. For M06 and M16, the grid resolutions (N_1, N_2, N_3, N_4) are $(2592, 1728, 1152, 576)$ and $(3456, 2592, 1152, 576)$, respectively. Changes in grid settings are managed using a third-order Lagrange polynomial interpolation. For $M_J = 1.6$, another DNS was conducted using a single grid setting of N_1 up to $t/T_J = 60$. By comparing turbulence statistics from this setup with others, we have confirmed that grid coarsening does not affect the flow evolution. The Kolmogorov scale is defined as $\eta = (\langle \mu \rangle / \langle \rho \rangle)^{3/4} \varepsilon^{-1/4}$ with the kinetic energy dissipation rate $\varepsilon = \langle \tau_{ij} S_{ij} \rangle / \langle \rho \rangle$, where S_{ij} is the rate-of-strain tensor. The spatial resolution is maintained at less than 1.1 times the Kolmogorov scale for M06 and less than 0.6 times for M16 after nearly HIT forms. A higher spatial resolution for the supersonic case is required to capture shocklets generated with large velocity fluctuations in an early time. This resolution for M16 was determined by the grid sensitivity test for isotropic turbulence with a high turbulent Mach number, where shocklets are generated by turbulent motion (Watanabe *et al.* 2021).

The integral scales of turbulence increase with time. At the end of the simulations, the longitudinal integral scales of the streamwise velocity, evaluated by integrating the auto-correlation function, are approximately $4D$ in M06 and $3D$ in M16. The side length of the cubic computational domain, $l = 60D$, is about 15 and 20 times larger than the integral scales in M06 and M16, respectively. A previous DNS study of decaying isotropic turbulence has suggested that the decay begins to be influenced by confinement effects when the domain size l is less than about three times the integral scale (Anas *et al.* 2020). The present DNS employs a domain size significantly larger than this threshold, ensuring that confinement effects are negligible.

3. Results and discussions

3.1. *Development of nearly homogeneous isotropic turbulence*

We first examine the development of turbulence arising from temporal jet interactions. Figure 2 visualises the local Mach number on a y–z plane at $t/T_J = 0$, 8 and 13 in M16. The initial condition, shown in figure 2(*a*), is characterised by jets, each exhibiting a circular distribution of high streamwise velocity. From the initial state, each jet transitions into a turbulent state in figure 2(*b*). The imprint of the jets remains visible at $t/T_J = 8$ as a non-uniform velocity distribution. However, as the jets interact with each other, the velocity of the initial jets becomes less pronounced by $t/T_J = 13$.

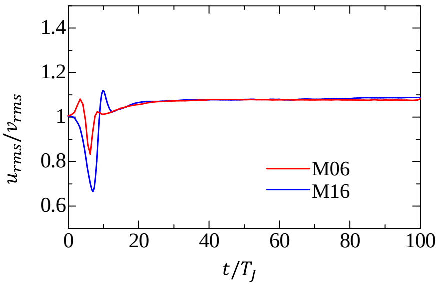

Figure 4: Temporal variations of the ratio between streamwise and lateral rms velocity fluctuations u_{rms}/v_{rms} at $(Y, Z) = (0, 0)$.

Figure 3(a) shows the temporal variations of the mean streamwise velocity, $\langle u \rangle$, at three locations. As illustrated in figure 1, $(Y/S, Z/S) = (0, 0)$ corresponds to the jet centre, while $(Y/S, Z/S) = (0.5, 0)$ and $(0.5, 0.5)$ are located between the jets. At $(Y/S, Z/S) = (0, 0)$, the potential core regime of the jet is characterised by a constant value of $\langle u \rangle / U_J = 1$, observed for $t/T_J \lesssim 5$ in M06 and $t/T_J \lesssim 7$ in M16. The turbulence development becomes slower as M_J increases, as expected from the delay in the turbulent transition of a supersonic jet (Bogdanoff 1983; Nagata *et al.* 2018). As the turbulent jets evolve, the mixing of high-speed jet fluid with low-speed ambient fluid progresses, resulting in a spatially uniform mean velocity distribution. This uniform mean flow is established at $t/T_J \approx 25$. Ghahremanian *et al.* (2014) conducted near-field measurements for 6×6 unconfined low-speed jets and observed that a nearly uniform mean velocity in a cross-sectional plane forms at a non-dimensionalised streamwise distance of approximately $x/D \approx 20$.

Figure 3(b) shows the rms fluctuations of the streamwise velocity, u_{rms}, at the same three locations. An initial rise in u_{rms} reflects the turbulence production associated with this non-uniform mean velocity. Following its peak, u_{rms} starts to decay. As u_{rms} decays from its peak, it becomes independent of the positions (Y, Z). The uniform distribution of $\langle u \rangle$ and u_{rms} is achieved before $t/T_J \approx 25$ for both M_J values. The evolution of the mean velocity and rms velocity aligns well with the experiments on nearly HIT generated by 6×6 unconfined low-speed jets (Ghahremanian *et al.* 2014). In the present DNS, the flow becomes statistically independent of positions on the the cross-sectional plane. Hereafter, the results at the jet center are presented.

Figure 4 shows the variations of the ratio between u_{rms} and v_{rms}. Once the mean streamwise velocity estabilishes the uniform distribution at $t/T_J \approx 25$, $u_{rms}/v_{rms} \approx 1.1$ hardly varies with time. Thus, nearly HIT has developed by the interaction of temporal jets. This value of $u_{rms}/v_{rms} \approx 1.1$ is consistent with observations in grid turbulence (Krogstad & Davidson 2010; Isaza *et al.* 2014; Kitamura *et al.* 2014). In addition, experiments on both confined and unconfined multiple jets have observed $u_{rms}/v_{rms} \approx 1.1$–$1.2$ (Ghahremanian *et al.* 2014; Mori *et al.* 2024).

Figure 5(a) shows the turbulent Reynolds number, $Re_\lambda = \langle \rho \rangle u_{rms} \lambda_x / \langle \mu \rangle$, calculated using the streamwise velocity. The Taylor microscale, λ_x, is defined as $\lambda_x = u_{rms}/(\partial u/\partial x)_{rms}$. The Reynolds number decays from its peaks, which are 89 in M06 and 107 in M16. The range of Re_λ remains within the low Re_λ regime, where turbulence decay is influenced by viscous effects, as observed in incompressible turbulence (Meldi & Sagaut 2013).

Figure 5(b) presents the turbulent Mach number, $M_T = \sqrt{u_{rms}^2 + v_{rms}^2 + w_{rms}^2}/\sqrt{\gamma R \langle T \rangle}$, where $\sqrt{\gamma R \langle T \rangle}$ is the speed of sound based on the mean temperature. As the mean temperature remains nearly constant over time, except during the initial transitional regime, the variation

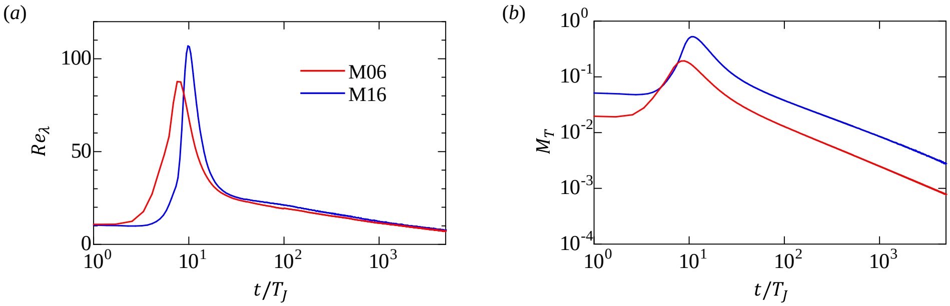

Figure 5: Temporal variations of (a) the turbulent Reynolds number Re_λ and (b) turbulent Mach number M_T at $(Y, Z) = (0, 0)$.

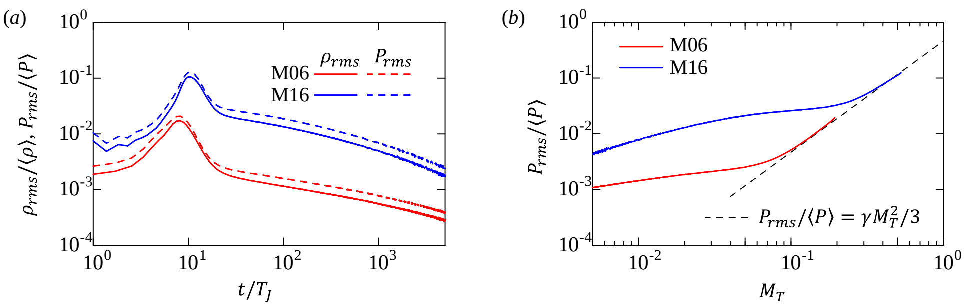

Figure 6: (a) Temporal variations of the rms fluctuations of density (ρ_{rms}) and pressure (P_{rms}), normalised by the mean density and mean pressure, respectively. (b) The dependence of the normalised rms pressure fluctuation on the turbulent Mach number (M_T). All results are evaluated at $(Y, Z) = (0, 0)$.

of M_T closely follows that of u_{rms}. The maximum values of M_T are 0.19 and 0.53 for M06 and M16, respectively, indicating that compressibility effects on turbulence are not negligible for M16. For a single jet at the same Mach number of 1.6, it has been shown that the temporally evolving supersonic jet initially generates pressure waves resembling spherical shock waves, characterised by strong compression followed by blunt expansion (Nagata *et al.* 2018). In the case of statistically steady isotropic turbulence subjected to solenoidal linear forcing, the statistical properties at small scales, such as the Re_λ dependence of velocity derivative skewness and flatness, are not affected by compressibility effects even at $M_T = 0.3$ (Watanabe *et al.* 2021). In M06, the maximum value of M_T remains below 0.2, indicating negligible compressibility effects due to turbulent velocity fluctuations, as will also be discussed below.

3.2. *Compressibity effects*

Figure 6(a) presents the rms values of density and pressure fluctuations, denoted ρ_{rms} and P_{rms}, respectively, at the jet centre. The rms fluctuations are normalised by the mean density $\langle\rho\rangle$ or mean pressure $\langle P\rangle$. The maximum values of ρ_{rms} and P_{rms} in M06 are less than 2 % of the mean density and pressure, respectively. During the decay of nearly HIT in M06, $\rho_{rms}/\langle\rho\rangle$ and $P_{rms}/\langle P\rangle$ are as small as 0.1 %, indicating that compressibility effects appear insignificant for this case. On the other hand, $\rho_{rms}/\langle\rho\rangle$ and $P_{rms}/\langle P\rangle$ increases up to about 10 % in M16. These highest fluctuations are observed in an early time, and both density and

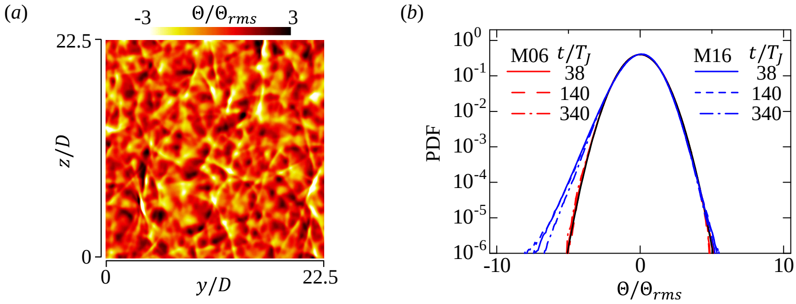

Figure 7: (*a*) Distribution of dilatation $\Theta = \partial u_i/\partial x_i$ on a y–z plane at $t/T_J = 80$ for M16. (*b*) The probability density function of Θ normalised by its rms value Θ_{rms}. The black line indicates the Gaussian distribution.

pressure fluctuations decay with time. As shown below, the shock waves are generated in an early time in M16, influencing turbulence at a later time by the long-time propagation.

Figure 6(*b*) plots $P_{rms}/\langle P\rangle$ as a function of the turbulent Mach number M_T. The DNS data is shown for the time period corresponding to the decay of M_T. In statistically steady isotropic turbulence subjected to solenoidal forcing (Wang *et al.* 2017; Watanabe *et al.* 2021), the normalised rms pressure fluctuations follow the relation:

$$P_{rms}/\langle P\rangle = A\gamma M_T^2/3, \tag{3.1}$$

with $A \approx 1$, as originally derived by Donzis & Jagannathan (2013). Figure 6(*b*) also illustrates this relation with $A = 1$. The turbulence generated by jet interaction in each case follows this relation at large M_T, which corresponds to the early period of the decay. Thus, (3.1) is valid for a short time after turbulence is generated by the jet interaction. Equation (3.1) provides a time-local relationship between pressure fluctuations and velocity fluctuations, assuming that pressure fluctuations at a given time are related to fluid motions at the same time. However, in decaying compressible turbulence, pressure waves, such as shock waves generated at an early time, decay more slowly than velocity fluctuations. As M_T decreases with time, (3.1) begins to underestimate $P_{rms}/\langle P\rangle$ because the pressure fluctuations at time $t = t_0$ can be partially influenced by turbulent motions at earlier times ($t < t_0$), when M_T was higher than at $t = t_0$. A similar non-local compressibility effect due to pressure wave propagation has been reported in the context of velocity gradient statistics (Yamamoto *et al.* 2022*b*).

The supersonic jets in M16 generate shock waves, which propagate in the periodic domain, even though M_T decays with time. Figure 7(*a*) visualises dilatation $\Theta = \partial u_i/\partial x_i = -(1/\rho)D\rho/Dt$ normalised by its rms value Θ_{rms} in M16. The visualised instance is $t/T_J = 80$, at which the turbulent Mach number is smaller than 0.1. Shock waves are identified as thin layers with large negative Θ, which indicate strong fluid compression. Figure 7(*b*) presents the probability density function (PDF) of Θ/Θ_{rms} from $t/T_J = 38$ to 340. The presence of shock waves affects the PDF of Θ, which is negatively skewed under the influence of shock waves because thin shock waves with large negative Θ occupy a small fraction of the flow. The PDF follows the Gaussian distribution in M06, where no shock waves propagate in turbulence. Negatively skewed distributions are observed in M06. The shape of PDF in M16 does not change with time, indicating that the shock waves propagate for long time, affecting the late-time behaviour of turbulence even at low M_T.

In the case of a single jet, the evolution of various velocity statistics in temporal simulations shows similarities to those observed in a spatial jet (da Silva & Pereira 2008; van Reeuwijk & Holzner 2014; Hayashi *et al.* 2021*b*). However, the interaction of temporal

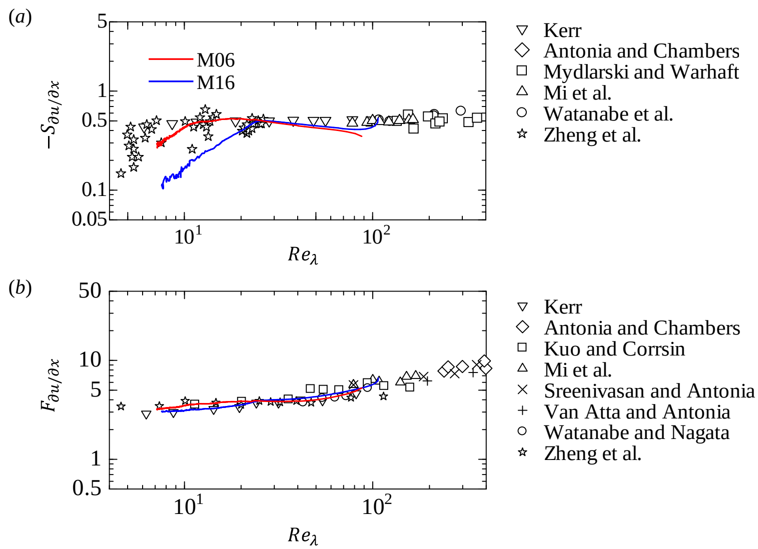

Figure 8: (*a*) Dependence of the velocity derivative skewness, $S_{\partial u/\partial x}$, on the turbulent Reynolds number Re_λ. The DNS results are taken at $(Y, Z) = (0, 0)$ after Re_λ reaches its peak. (*b*) Dependence of the velocity derivative flatness, $F_{\partial u/\partial x}$, on Re_λ. The DNS results are taken at $(Y, Z) = (0, 0)$ after Re_λ reaches its peak. The figure includes data from studies of incompressible turbulence (Kerr 1985; Kuo & Corrsin 1971; Antonia & Chambers 1980; Van Atta & Antonia 1980; Mydlarski & Warhaft 1996; Sreenivasan & Antonia 1997; Watanabe & Nagata 2018; Mi *et al.* 2013; Watanabe *et al.* 2019; Zheng *et al.* 2021).

supersonic jets exhibits notable differences compared to the wind tunnel experiments. In the experiments, a counter pressure gradient, observed before a homogeneous mean flow fully develops due to jet interaction, causes a deceleration of the mean flow, associated with a weak compression (Mori *et al.* 2024). This deceleration is not observed in the temporal jets. Moreover, shock wave propagation in the wind tunnel is influenced by the test section walls, which cause the waves to reflect. This wave reflection does not occur in DNS due to periodic boundary conditions. However, wave propagation from the near-nozzle region toward the decay region in the wind tunnel bears similarity to that from early to late times in temporal simulations. Both spatial and temporal jets produce turbulence through the mean shear associated with the non-uniform mean velocity of the jets. The cross-sectional distribution of mean shear is virtually identical for both spatial and temporal jets.

Figure 8 plots the skewness, $S_{\partial u/\partial x} = \langle(\partial u'/\partial x)^3\rangle/\langle(\partial u'/\partial x)^2\rangle^{3/2}$, and flatness, $F_{\partial u/\partial x} = \langle(\partial u'/\partial x)^4\rangle/\langle(\partial u'/\partial x)^2\rangle^2$, of the longitudinal velocity gradient $\partial u/\partial x$ as functions of Re_λ. The results are shown after Re_λ reaches its peak and are compared with previous studies of incompressible turbulence. The flatness values in both M06 and M16 align well with those of incompressible turbulence at comparable Re_λ, decreasing as Re_λ declines with turbulence decay. Experiments and DNS have shown that statistically steady compressible turbulence tends to exhibit higher flatness values than incompressible turbulence (Donzis & John 2020; Watanabe *et al.* 2021; Yamamoto *et al.* 2022*a*). However, this trend is not observed in the present DNS of decaying turbulence. The dependence on Mach number is more pronounced for the skewness. It is known that skewness plotted against Re_λ shows more flow dependence than flatness, even in incompressible turbulence (Zheng *et al.* 2021). In M06, $-S_{\partial u/\partial x}$ decreases significantly for $Re_\lambda \lesssim 10$, consistent with grid turbulence data reported in Zheng *et al.* (2021). In M16, this decrease occurs at larger Re_λ, and $-S_{\partial u/\partial x}$ tends to be

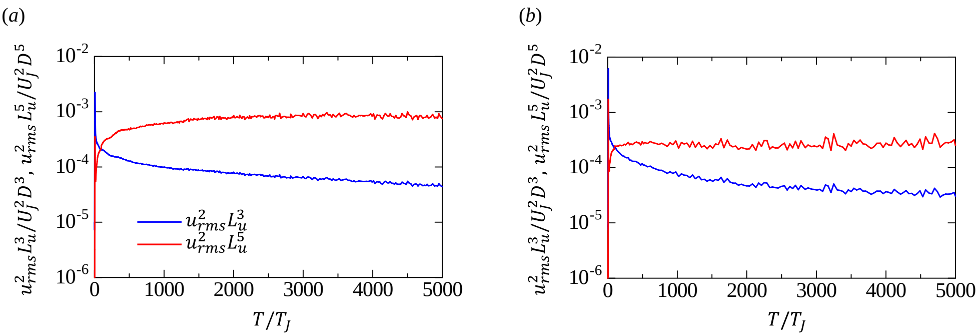

Figure 9: Temporal variations of $u_{rms}^2 L_u^3$ and $u_{rms}^2 L_u^5$ in (*a*) M06 and (*b*) M16.

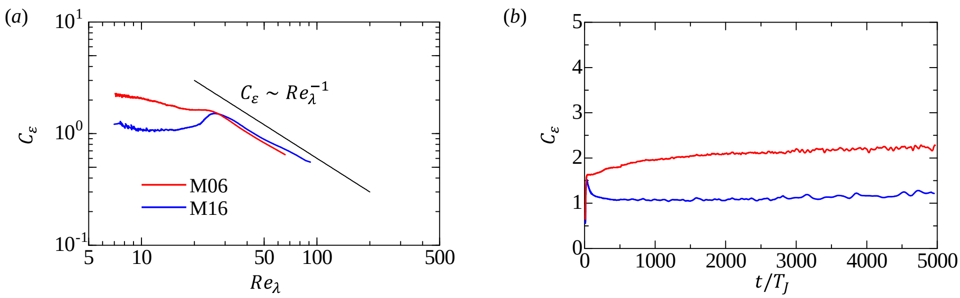

Figure 10: (*a*) Dependence of the non-dimensional energy dissipation rate, C_ε, on the turbulent Reynolds number, Re_λ. (*b*) Temporal variations of C_ε. The data is taken for the period following the peak of Re_λ.

smaller than in M06. This reduction in $-S_{\partial u/\partial x}$ due to compressibility effects has been reported in other DNS studies of decaying compressible turbulence, although it has received limited attention (Li *et al.* 2010; Samtaney *et al.* 2001). While Samtaney *et al.* (2001) also found that decaying compressible turbulence with high initial M_T has smaller $-S_{\partial u/\partial x}$ values than low-M_T cases, the difference is less significant than in the present DNS. In Samtaney *et al.* (2001), DNS was conducted over a period of less than 10 times the integral time scale. In contrast, the present DNS covers a much longer duration, over 2000 times the integral time scale at the time of maximum Re_λ, which might explain the larger deviation of $-S_{\partial u/\partial x}$ in M16 from incompressible flow data.

3.3. *Decay properties and energy spectra*

The decay laws of (1.1) and (1.2) are based on the invariance of $u_{rms}^2 L_u^5$ and $u_{rms}^2 L_u^3$ during the decay, respectively, under the assumption of self-similarity at large scales. Here, L_u denotes the longitudinal integral scale of u. At a given time, L_u is evaluated using the auto-correlation function of u, $f_u(r_x, Y, Z) = \langle u'(x, Y, Z)u'(x + r_x, Y, Z)\rangle/u_{rms}^2(Y, Z)$, as $L_u(Y, Z) = \int_0^{r_{x0}} f_u(r_x, Y, Z)dr_x$, where r_{x0} is the r_x value at which f_u first crosses zero. Figure 9 shows the temporal variations of $u_{rms}^2 L_u^5$ and $u_{rms}^2 L_u^3$ for both Mach number cases. Nearly HIT develops by approximately $t/T_J = 25$. However, both $u_{rms}^2 L_u^5$ and $u_{rms}^2 L_u^3$ vary with time even after turbulence generation. In the present DNS, $u_{rms}^2 L_u^3$ decreases consistently over time until $t/T_J = 5000$ for both cases. Conversely, $u_{rms}^2 L_u^5$ becomes nearly time-independent at later times, particularly after $t/T_J \approx 2000$ for M06 and $t/T_J \approx 500$ for

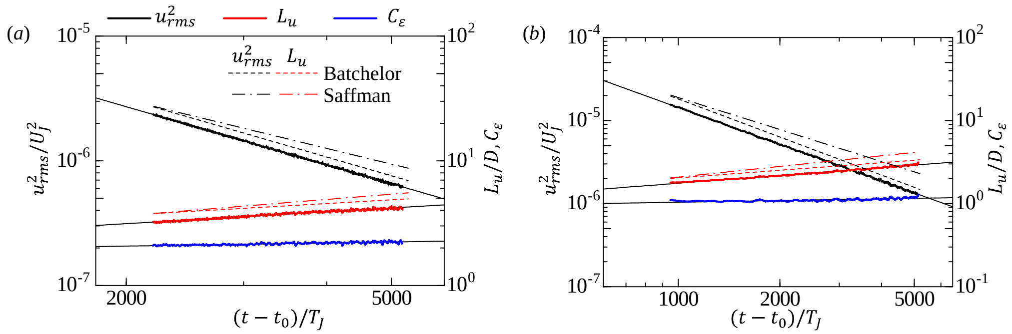

Figure 11: Temporal variations of u_{rms}^2, L_u and C_ε over time: (*a*) M06; (*b*) M16. Thin black solid lines indicate power laws with exponents determined using the least squares method. Dashed and dash-dot line lines represent the power laws for u_{rms}^2 and L_u with the exponents for Batchelor and Saffman turbulence.

M16. The variations of $u_{rms}^2 L_u^5$ observed in the present DNS are consistent with findings from previous studies on decaying isotropic turbulence initialised with an energy spectrum $E(k) \sim k^4$. The DNS results of Ishida *et al.* (2006) indicate that in such cases, $u_{rms}^2 L_u^5$ increases over time before reaching a constant value. In addition, grid turbulence exhibits a similar behaviour (Watanabe & Nagata 2018): $u_{rms}^2 L_u^3$ becomes time-independent only after the flow has evolved for a sufficiently long time in a nearly homogeneous and isotropic state. For $t/T_J \geqslant 2000$, the least squares method yields $u_{rms}^2 L_u^5/U_J^2 D^5 \sim (t/T_J)^{0.038}$ and $u_{rms}^2 L_u^3/U_J^2 D^3 \sim (t/T_J)^{-0.561}$ for M06. Similarly, the results for M16 yield $u_{rms}^2 L_u^5/U_J^2 D^5 \sim (t/T_J)^{0.021}$ and $u_{rms}^2 L_u^3/U_J^2 D^3 \sim (t/T_J)^{-0.533}$. Thus, $u_{rms}^2 L_u^5$ exhibits a weaker time dependence than $u_{rms}^2 L_u^3$, suggesting that the decay law of Batchelor turbulence is valid.

Figure 10 plots $C_\varepsilon = \varepsilon/(u_{rms}^3/L_u)$ as a function of Re_λ or time. Initially, C_ε exhibits an increase with time, following the scaling $C_\varepsilon \sim Re_\lambda^{-1}$ of non-equilibrium turbulence (Valente & Vassilicos 2014). This scaling near the nozzles has also been observed in the near-field of grid turbulence (Valente & Vassilicos 2014; Mora *et al.* 2019) as well as the near field of turbulence generated by the jet interaction (Mori *et al.* 2024). In M06, a gradual increase in C_ε continues beyond the non-equilibrium phase due to the low Re_λ effects. Conversely, in M16, C_ε declines after the non-equilibrium phase is over. Shock wave propagation, from an early time with large M_T in M16, amplifies velocity fluctuations and reduces integral scales, potentially contributing to the observed decrease in C_ε (Kitamura *et al.* 2017; Tanaka *et al.* 2018). Such deviations in small-scale statistics from incompressible values are also documented for inhomogeneous or decaying compressible turbulence (Samtaney *et al.* 2001; Xinliang *et al.* 2002; Yamamoto *et al.* 2022*a*).

The decay properties are investigated during the phase with nearly constant $u_{rms}^2 L_u^5$, to compare the variations of u_{rms} and L_u with theoretical predictions. The examined time intervals are $2000 \leqslant t/T_J \leqslant 5000$ for M06 and $800 \leqslant t/T_J \leqslant 5000$ for M16. Additionally, a sensitivity test for the fitting range is provided below. The present study considers the following power laws:

$$u_{rms}^2 \sim (t-t_0)^n, L_u \sim (t-t_0)^{n_L}, C_\varepsilon \sim (t-t_0)^{n_C}, \tag{3.2}$$

where t_0 is the virtual origin. The value of t_0 is determined from the decay of u_{rms}^2. Following the methodology in a previous study, a linear least squares method is applied with a predetermined t_0 that minimises the fitting error for u_{rms}^2 (Watanabe *et al.* 2022). Specifically, the fitting for $(t-t_0, u_{rms}^2)$ using the linear least squares method is iteratively

Table 1: The power law exponents for u_{rms}^2, L_u and C_ε, denoted as n, n_L and n_C, respectively, and the virtual origin t_0. The theoretical values of Batchelor and Saffman turbulence for n and n_L are denoted by superscripts (B) and (S), respectively. The relative differences between the DNS results and the theoretical predictions are calculated as: $\Delta n^{(\alpha)} = (n - n^{(\alpha)})/n^{(\alpha)}$ and $\Delta n_L^{(\alpha)} = (n_L - n_L^{(\alpha)})/n_L^{(\alpha)}$, where $\alpha = B$ for Batchelor turbulence and $\alpha = S$ for Saffman turbulence.

Run	t_0/T_J	n	n_L	n_C	$n^{(B)}$	$n^{(S)}$	$n_L^{(B)}$	$n_L^{(S)}$	$\Delta n^{(B)}$	$\Delta n^{(S)}$	$\Delta n_L^{(B)}$	$\Delta n_L^{(S)}$
M06	−191.9	−1.551	0.316	0.083	−1.547	−1.299	0.309	0.433	−0.3%	−19.4%	2.0%	−27.1%
M16	−142.1	−1.469	0.312	0.066	−1.522	−1.279	0.304	0.426	3.5%	−14.9%	2.4%	−26.9%

performed by varying t_0 between $-300T_J \leqslant t_0 \leqslant 300T_J$ with an increment of $0.1T_J$. The t_0 value that minimises the error is selected and used to determine the power law exponents (n, n_L, n_C). This approach has been shown to yield decay exponents comparable to those obtained using a non-linear least squares method (Levenberg–Marquardt algorithm), which directly determines (t_0, n) from the data (t, u_{rms}^2) (Watanabe *et al.* 2022). The values of t_0 determined here are also utilised in the subsequent analysis. A least squares method is applied to analyse L_u and C_ε, thereby determining the power law exponents n_L and n_C. Figure 11 presents the variations of u_{rms}^2, L_u and C_ε with $t - t_0$, compared with the power laws (thin black solid lines) using the exponents evaluated by the described method. The variations of these quantities are well approximated by the power laws. When confinement effects due to a finite computational domain become significant, the decay of u_{rms}^2 accelerates (Anas *et al.* 2020). In the present study, such confinement-induced acceleration is not observed in the decay of u_{rms}^2.

Table 1 summarises the virtual origin t_0 and the power law exponents (n, n_L, n_C), comparing them with the theoretical predictions for Saffman and Batchelor turbulence. The theoretical values from (1.1) and (1.2) are evaluated using the DNS-derived values of n_C and are denoted as $(n^{(B)}, n_L^{(B)})$ for Batchelor turbulence, and $(n^{(S)}, n_L^{(S)})$ for Saffman turbulence. The behaviour of $u_{rms}^2 L_u^5$ and $u_{rms}^2 L_u^3$ indicates that the decay aligns with the Batchelor turbulence theory. For both Mach number cases, n and n_L closely match the values predicted for Batchelor turbulence. The table also includes the relative differences between the exponents and the theoretical values, defined as: $\Delta n^{(\alpha)} = (n - n^{(\alpha)})/n^{(\alpha)}$, and $\Delta n_L^{(\alpha)} = (n_L - n_L^{(\alpha)})/n_L^{(\alpha)}$, where $\alpha = B$ (Batchelor) or S (Saffman). For Batchelor turbulence, the relative difference in exponents is less than 4%, while for Saffman turbulence, the differences are approximately 15–27% for u_{rms}^2 and L_u. As also visualised in figure 11, the theory for Saffman turbulence predicts a slower decay of u_{rms}^2 and a faster growth of L_u than the DNS results. Although the exponents (n, n_L) in both M06 and M16 are evaluated during the period with nearly constant $u_{rms}^2 L_u^5$, (n, n_L) differ between these two cases. This difference is attributed to the variation of C_ε. Thus, compressibility effects influence the decay laws through C_ε. These findings suggest that the turbulence decay in the jet interaction follows the Batchelor turbulence theory. Appendix A provides comparisons of the decay exponents with the theories of Batchelor and Saffman turbulence using experimental data available in the literature (Tan *et al.* 2023; Mori *et al.* 2024). The exponents evaluated in these studies are also consistent with the predictions of Batchelor turbulence. However, these experiments provided measurement results over a limited range of streamwise positions.

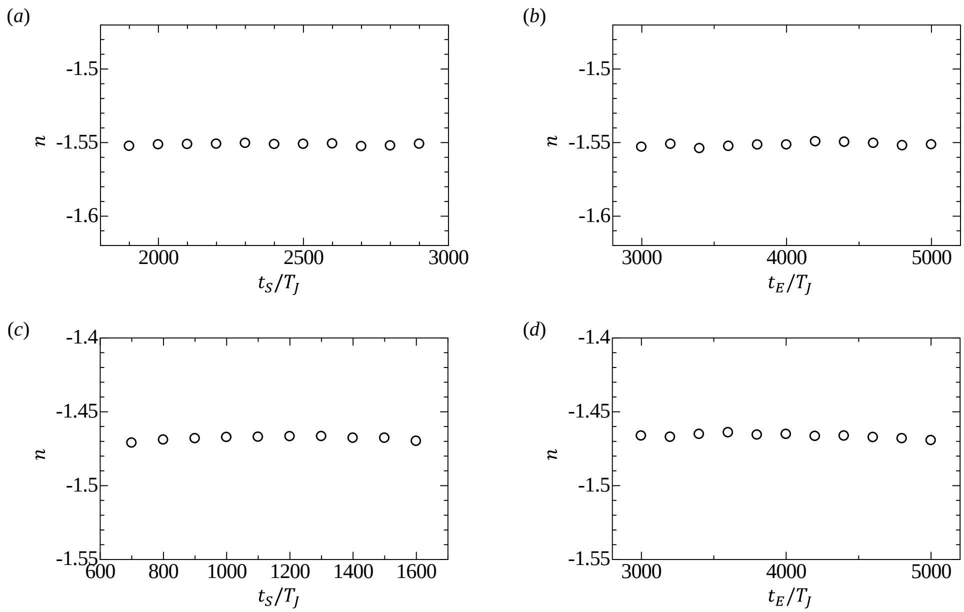

Figure 12: Dependence of the decay exponent n of u_{rms}^2 on the fitting range $t_S \leqslant t \leqslant t_E$: ($a$) t_S dependence with $t_E = 5000T_J$ fixed in M06; (b) t_E dependence with $t_S = 2000T_J$ fixed in M06; (c) t_S dependence with $t_E = 5000T_J$ fixed in M16; (d) t_E dependence with $t_S = 800T_J$ fixed in M16.

Further experimental investigations are encouraged to comprehensively assess the decay of turbulence generated by jet interactions.

Figure 12 examines the dependence of the decay exponent n of u_{rms}^2 on the fitting range $t_S \leqslant t \leqslant t_E$, with varying t_S or t_E. The decay exponents only slightly vary between -1.554 and -1.549 for M06 in figures 12(a, b) and between -1.472 and -1.464 for M16 in figures 12(c, d), depending on the choice of t_S and t_E. This demonstrates that the selection of the fitting range hardly affects the evaluation of the decay exponent. Additionally, different virtual origins from those determined above were tested. Changing the virtual origin by 10% resulted in a change of the decay exponent n by less than 2%. This weak dependence on the virtual origin is partly attributed to the fitting range encompassing much larger t values compared to t_0, a phenomenon also observed in grid turbulence (Watanabe *et al.* 2022).

Figure 13 presents the three-dimensional energy spectrum $E(k)$ during the decay. The calculation of $E(k)$ employs the shell averaging method in wavenumber space (Valente *et al.* 2016). For comparisons with $E(k) \sim k^4$ and k^2, $E(k)$ is multiplied by k^{-4} or k^{-2} so that these power laws appear as horizontal lines. For both Mach numbers, $k^{-4}E$ tends toward a constant value and $k^{-2}E$ decreases following $k^{-2}E \sim k^2$ as k becomes small, indicating that the energy spectrum at small wavenumbers follows a k^4 scaling rather than k^2. This behaviour confirms the formation of Batchelor turbulence. The spectral slope within the k^4 range remains consistent over time, with small variations related to statistical convergence. The formation of $E(k) \sim k^4$ occurs earlier than the invariance of $u_{rms}^2 L_u^5$ observed in figure 9. It should be noted that $E(k) \sim k^4$ is not a sufficient condition for the constancy of $u_{rms}^2 L_u^5$ in Batchelor turbulence. In DNS of decaying isotropic turbulence, where the flow is initialised with a prescribed spectral shape of $E(k) \sim k^4$, $u_{rms}^2 L_u^5$ becomes time-independent only after the turbulence evolves over a certain period (Ishida *et al.* 2006). This behaviour is consistent with the turbulence generated by jet interactions observed in the present study.

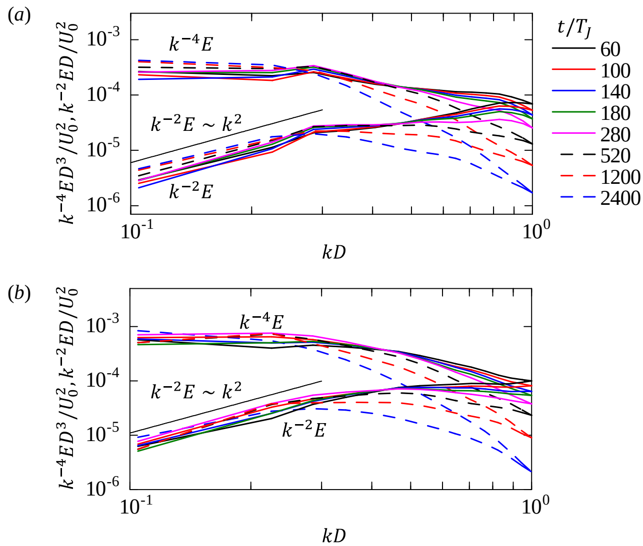

Figure 13: Temporal evolutions of the three-dimensional energy spectrum, $E(k)$, for (*a*) M06 and (*b*) M16. The spectra are premultiplied by k^{-4} or k^{-2} to facilitate comparison with $E(k) \sim k^4$ of Batchelor turbulence and $E(k) \sim k^2$ of Saffman turbulence.

4. Conclusion

DNS is performed to investigate the interaction of temporally evolving circular jets with jet Mach numbers $M_J = 0.6$ and 1.6, and a jet Reynolds number of 3000. For both cases, the jet interaction leads to the formation of nearly HIT, with the ratio of streamwise to transverse rms velocity fluctuations around 1.1, although the turbulent transition is delayed in the higher M_J case. The rms pressure fluctuations, P_{rms}, normalised by the mean pressure, decrease as the turbulent Mach number decreases. Their relationship shortly after turbulence generation is well described by (3.1), which is often applied to statistically steady isotropic turbulence, although it underestimates P_{rms} after the turbulence has sufficiently decayed. In the $M_J = 1.6$ case, the turbulent Mach number becomes sufficiently high to generate shock waves, confirmed by the negatively skewed probability distribution of dilatation. These shock waves propagate through the turbulence over a long period and continue to affect the flow at later times, even after the turbulent Mach number decreases. Consistent with previous studies of decaying compressible turbulence (Li *et al.* 2010; Samtaney *et al.* 2001), the magnitude of the velocity derivative skewness is smaller for $M_J = 1.6$ than for $M_J = 0.6$. Additionally, the non-dimensional dissipation rate C_ε is lower for $M_J = 1.6$. Thus, the statistical properties of small-scale motions are altered by compressibility effects. The late-time decay of turbulence is consistent with Batchelor turbulence theory. For the rms velocity fluctuations u_{rms} and the integral scale L_u of the streamwise velocity, $u_{rms}^2 L_u^5$ remains nearly constant over time, while $u_{rms}^2 L_u^3$ continuously decreases, indicating that the turbulence follows Batchelor turbulence theory. The power-law exponents of u_{rms}^2 and L_u are also consistent with the theoretical predictions for Batchelor turbulence, with corrections due to the temporal variation of C_ε. The three-dimensional energy spectrum further supports this, exhibiting $E(k) \sim k^4$ for small k assumed in Batchelor turbulence. This k^4 spectral shape develops even before $u_{rms}^2 L_u^5$ becomes nearly constant. These behaviours, consistent with Batchelor turbulence, are observed even for $M_J = 1.6$, where small-scale turbulence characteristics deviate from incompressible flows due to compressibility effects.

The modulations of small-scale motions, such as shock wave propagation, appear to have little influence on the decay laws determined by the large-scale flow characteristics. The present numerical simulations provide new insights and encourage further experimental investigations into Batchelor turbulence generated by jet interactions.

Acknowledgements. DNS were performed using the high-performance computing systems at the Japan Agency for Marine-Earth Science and Technology and Nagoya University. This work was supported by Collaborative Research Project on Computer Science with High-Performance Computing in Nagoya University.

Funding. This work was supported by JSPS KAKENHI Grant Nos. JP22K03903 and JP22H01398.

Declaration of interests. The authors report no conflict of interest.

Data availability statement. The data that support the findings of this study are available from the corresponding author upon reasonable request.

Appendix A. Experimental studies of decaying turbulence generated by jet interaction

The interaction of jets has also been investigated in early studies of turbulence generated by jet grids, which consist of a conventional grid combined with a nozzle array (Gad-el Hak & Corrsin 1974). In these setups, jets are injected from the grid into a coflow. However, in most experiments, the jets operate at very low flow rates, resulting in turbulence generation dominated by the grid itself. An exception is the study by Tan *et al.* (2023), which examined jet grids with a very weak coflow, where turbulence is primarily generated by the jets. Similarly, Mori *et al.* (2024) reported experiments on turbulence generated by the interaction of numerous supersonic jets, which decay within a confined test section. In this appendix, we analyse the measurement results from these studies. Fundamental velocity statistics related to homogeneity and isotropy were reported in the original studies (Tan *et al.* 2023; Mori *et al.* 2024; Watanabe *et al.* 2024). The mean velocity generated by continuous jet interactions becomes homogeneous within the test section. These studies examined parallel jets issued into a test section, the end of which functions as an outlet. Consequently, the mean velocity profile is unlikely to be influenced by large-scale circulations, which may play a significant role when continuous jets are issued into a closed vessel. Other experiments on HIT generated by jet interaction have been conducted using unsteady-jet generators (Hwang & Eaton 2004; Variano *et al.* 2004; Bellani & Variano 2014; Carter *et al.* 2016; Pérez-Alvarado *et al.* 2016; Yamamoto *et al.* 2022*b*). However, the interaction of unsteady jets generates turbulence differently from continuous jets. In continuous jets, temporal velocity fluctuations are initially produced by shear instability arising from the mean shear. In contrast, unsteady jets generate velocity fluctuations directly through their operational variations. Since the decay of HIT strongly depends on the turbulence generation mechanism, we focus on the interaction of continuous jets.

First, we examine the velocity data measured in the vertical octagonal non-corrosive stirred energetic turbulence (V-ONSET) facility reported in Tan *et al.* (2023). Velocity measurements using particle image velocimetry were conducted for a nozzle spacing of $S = 40$ mm and a nozzle diameter of $D = 5$ mm. A square grid with jet holes was installed in a water tunnel with an octagonal cross-section test section. Jets were issued from the grid at a velocity of 5.5 m/s within a coflow at 0.27 m/s. The measurements covered a streamwise distance x normalised by the jet diameter D within $53 \leqslant x/D \leqslant 165$. As observed in the present DNS, their measurements confirmed the generation of nearly HIT decaying within the test section, where a power-law decay was observed for u_{rms}. The integral scale, evaluated with the auto-correlation function, was not available in this study. Therefore, the discussion focuses solely on the decay of u_{rms}^2. The parameters in the scaling $u_{rms}^2 \sim (x - x_0)^n$ were determined with the same method as in the present DNS, using a linear least squares method with a predetermined virtual origin x_0 to minimise the fitting error. Their data yielded $x_0 = 2.5D$ and $n = -2.2$, with the nozzle diameter D. In decaying HIT, the relation $u_{rms}^2 \sim (x - x_0)^n$ implies $\varepsilon \sim (x - x_0)^{(n-1)}$, where ε is the dissipation rate. The turbulent Reynolds number, $Re_\lambda = u_{rms}\lambda/\nu$, defined with the Taylor microscale $\lambda = u_{rms}\sqrt{15\nu/\varepsilon}$, evolves as $Re_\lambda \sim (x-x_0)^{(n+1)/2}$. The measurements were conducted in the near-nozzle region of $53 \leqslant x/D \leqslant 165$. In turbulence generated by jet interaction in this range, C_ε increases as turbulence decays, following the non-equilibrium dissipation scaling (Mori *et al.* 2024). In this non-equilibrium region, where $C_\varepsilon \sim Re_\lambda^{-1}$, it follows that $C_\varepsilon \sim (x - x_0)^{-(n+1)/2}$. The power law decay of u_{rms}^2 with $n = -2.2$ predicts $C_\varepsilon \sim (x - x_0)^{0.6}$. With this exponent for C_ε, (1.1) and (1.2) predict $n = -2.3$ for Batchelor turbulence and $n = -1.9$ for Saffman turbulence. The experimentally derived exponent $n = -2.2$ closely aligns with the Batchelor turbulence theory. Although this analysis assumes non-equilibrium turbulence, which is not explicitly verified in their experimental data, the jet grid used in Tan *et al.* (2023) likely generates turbulence consistent with the theory of Batchelor turbulence.

Additionally, the velocity data measured in the multiple-jet wind tunnel described in Mori *et al.* (2024) is examined here. This dataset was also analysed in Watanabe *et al.* (2024). These papers include various velocity statistics, comparisons with other turbulent flows and uncertainty tests. This facility generates decaying, nearly HIT through the interaction of 6×6 parallel supersonic jets within a test section of 1 m length and a cross-section of 0.01×0.01 m^2. The nozzle diameter is $D = 4.31$ mm and the nozzle spacing is $S = 12$ mm. Velocity measurements using particle tracking velocimetry (PIV) were conducted for ideally-expanded, supersonic parallel jets with a jet Mach number of $M_J = 1.36$ and a jet Reynolds number of $Re_J = 1.9 \times 10^5$. The measurements were conducted for $25 \leqslant x/D \leqslant 180$. The experiments in the nearly HIT region were conducted repeatedly until approximately 700 statistically-independent vector profiles were collected. Velocity statistics are evaluated by taking ensemble averages. It was observed that nearly HIT forms before $x/D \approx 80$. As the integral scale grows with the decay of turbulence, the test-section side wall causes confinement effects on turbulence. Beyond $x/D \approx 140$, the confinement effects become prevalent, halting the increase in the integral scale and accelerating the decay of velocity fluctuations, as also observed in decaying HIT with confinement effects (Skrbek & Stalp 2000; Morize & Moisy 2006). Consequently, decay properties are analysed within the range of $81 \leqslant x/D \leqslant 139$. Because turbulence decays along the streamwise direction, the spatial longitudinal auto-correlation function of u is assessed using two statistically different points from PIV data, complicating interpretation. Therefore, the present study focuses on the statistics of v. The longitudinal auto-correlation function of v is evaluated using ensemble and spatial averages to mitigate statistical errors. Within each PIV measurement area, the correlation function is computed at eight streamwise locations, spaced equidistantly. Spatial averages for f_v are calculated over a length of approximately $2S$ in the x direction and over the full height of the measurement area in the y direction. The integral of f_v provides the integral scale L_v.

The energy dissipation rate ε was evaluated from the decay of TKE, $k_T = (u_{rms}^2 + 2v_{rms})/2$ with the TKE transport equation in decaying HIT and the non-dimensional dissipation rate was assessed as $C_\varepsilon = \varepsilon/(v_{rms}^3/L_v)$, as detailed in Mori *et al.* (2024). Here, the streamwise gradient of k_T, $\partial k_T/\partial x$ is evaluated by fitting a power law to $k_T(x)$ in a dimensional form, and is used to assess ε with the TKE equation. The evaluation ε is validated by comparing the inertial range statistics normalized ε and kinematic viscosity with other turbulent flows (Mori *et al.* 2024; Watanabe *et al.* 2024). Figure 14 depicts the variations of

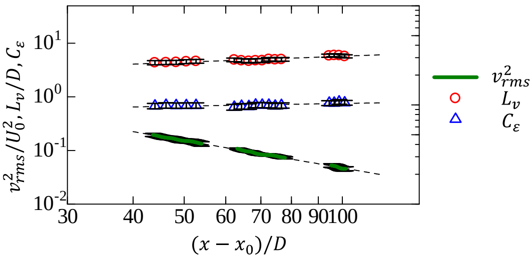

Figure 14: Streamwise variations of velocity variance v_{rms}^2, integral scale L_v and non-dimensional dissipation rate C_ε. The error bars indicate possible statistical errors estimated with reduced samples.

v_{rms}^2, L_v and $C_\varepsilon = \varepsilon/(v_{rms}^3/L_v)$ as functions of $(x-x_0)/D$, where x_0 is the virtual origin of the TKE decay. Possible statistical errors are evaluated by dividing staistical samples randomly into two datasets, whose root-mean-squared differences in the statistical quantities are shown as error bars, as detailed in Mori *et al.* (2024). The virtual origin is determined by applying the same method used to the present DNS data. A least squares method is employed to determine the power-law exponents for $v_{rms}^2 \sim (x-x_0)^n$, $L_v \sim (x-x_0)^{n_L}$ and $C_\varepsilon \sim (x-x_0)^{n_C}$, resulting in $n = -1.70$, $n_L = 0.36$ and $n_C = 0.16$. The streamwise increase in C_ε is most likely attributable to non-equilibrium turbulence, as shown in the plot of $(Re_\lambda, C_\varepsilon)$ in Mori *et al.* (2024) and by the present DNS. With $n_C = 0.16$, the theories of Batchelor and Saffman turbulence, (1.1, 1.2), predict $(n, n_L) = (-1.66, 0.33)$ and $(-1.39, 0.47)$, respectively. These exponents indicate $v_{rms}^2 L_v^5 \sim (x-x_0)^{0.10}$ and $v_{rms}^2 L_v^3 \sim (x-x_0)^{-0.62}$. As observed in the present DNS, $v_{rms}^2 L_v^5$ weakly depends on the streamwise position, while $v_{rms}^2 L_v^3$ continuously declines. Therefore, the decay of turbulence generated by jet interaction aligns with the Kolmogorov decay law of Batchelor turbulence.

These two experimental studies have provided measurement results for a limited range of streamwise locations, although they do not contradict the far-field decay observed in the present DNS. The decay properties are likely influenced by how turbulence is generated and depend on various parameters such as jet Reynolds and Mach numbers, as well as jet nozzle arrangements. The findings of this study highlight the need for further experimental investigations into jet interactions.

REFERENCES

Anas, M., Joshi, P. & Verma, M. K. 2020 Freely decaying turbulence in a finite domain at finite Reynolds number. *Phys. Fluids* **32** (9).

Anderson, E. A. & Spall, R. E. 2001 Experimental and numerical investigation of two-dimensional parallel jets. *J. Fluids Eng.* **123** (2), 401–406.

Antonia, R. A. & Chambers, A. J. 1980 On the correlation between turbulent velocity and temperature derivatives in the atmospheric surface layer. *Bound.-Layer Meteor.* **18**, 399–410.

Batchelor, G. K. & Proudman, I. 1956 The large-scale structure of homogeneous turbulence. *Phil. Trans. R. Soc. A* **248**, 369–405.

Batchelor, G. K. & Townsend, A. A. 1948 Decay of turbulence in the final period. *Proc. Roy. Soc. A.* **194** (1039), 527–543.

Bellani, G. & Variano, E. A. 2014 Homogeneity and isotropy in a laboratory turbulent flow. *Exp. Fluids* **55**, 1–12.

Blakeley, B. C., Olson, B. J. & Riley, J. J. 2022 Self-similarity of scalar isosurface area density in a temporal mixing layer. *J. Fluid Mech.* **951**, A44.

Bogdanoff, D. W. 1983 Compressibility effects in turbulent shear layers. *AIAA J.* **21** (6), 926–927.

BORNOFF, R. B. & MOKHTARZADEH-DEHGHAN, M. R. 2001 A numerical study of interacting buoyant cooling-tower plumes. *Atmos. Environ.* **35** (3), 589–598.

BOUSSOUFI, M., SABEUR-BENDEHINA, A., OUADHA, A., MORSLI, S. & EL GANAOUI, M. 2017 Numerical analysis of single and multiple jets. *Eur. Phys. J.: Appl. Phys.* **78** (3), 34814.

BURR, JASON R & KEN, H YU 2019 Experimental characterization of RDE combustor flowfield using linear channel. *Proc. Combust. Inst.* **37** (3), 3471–3478.

CALISKAN, S., BASKAYA, S. & CALISIR, T. 2014 Experimental and numerical investigation of geometry effects on multiple impinging air jets. *Int. J. Heat Mass Transfer* **75**, 685–703.

CARTER, D., PETERSEN, A., AMILI, O. & COLETTI, F. 2016 Generating and controlling homogeneous air turbulence using random jet arrays. *Exp. Fluids* **57**, 1–15.

COLTRIN, I. S., BLOTTER, J. D., MAYNES, R. D. & GEE, K. L. 2013 Shock-cell structures and corresponding sound pressure levels emitted from closely spaced supersonic jet arrays. *Appl. Acoust.* **74** (12), 1519–1526.

COLTRIN, I. S., MAYNES, R. D., BLOTTER, J. D. & GEE, K. L. 2014 Influence of nozzle spacing and diameter on acoustic radiation from supersonic jets in closely spaced arrays. *Appl. Acoust.* **81**, 19–25.

DAVIDSON, P. A. 2004 *Turbulence: An Introduction for Scientists and Engineers*. Oxford Univ. Pr.

DAVIDSON, P. A., OKAMOTO, N. & KANEDA, Y. 2012 On freely decaying, anisotropic, axisymmetric Saffman turbulence. *J. Fluid Mech.* **706**, 150–172.

DIAMESSIS, P. J., SPEDDING, G. R. & DOMARADZKI, J. A. 2011 Similarity scaling and vorticity structure in high-Reynolds-number stably stratified turbulent wakes. *J. Fluid Mech.* **671**, 52–95.

DONZIS, D. A. & JAGANNATHAN, S. 2013 Fluctuations of thermodynamic variables in stationary compressible turbulence. *J. Fluid Mech.* **733**, 221–244.

DONZIS, D. A. & JOHN, J. P. 2020 Universality and scaling in homogeneous compressible turbulence. *Phys. Rev. Fluids* **5** (8), 084609.

FREUND, J. B., LELE, S. K. & MOIN, P. 2000 Compressibility effects in a turbulent annular mixing layer. Part 1. turbulence and growth rate. *J. Fluid Mech.* **421**, 229–267.

GAMPERT, M., BOSCHUNG, J., HENNIG, F., GAUDING, M. & PETERS, N. 2014 The vorticity versus the scalar criterion for the detection of the turbulent/non-turbulent interface. *J. Fluid Mech.* **750**, 578–596.

GEERS, L. F. G., HANJALIĆ, K. & TUMMERS, M. J. 2006 Wall imprint of turbulent structures and heat transfer in multiple impinging jet arrays. *J. Fluid Mech.* **546**, 255–284.

GEERS, L. F. G., TUMMERS, M. J. & HANJALIĆ, K. 2005 Particle imaging velocimetry-based identification of coherent structures in normally impinging multiple jets. *Phys. Fluids* **17** (5).

GHAHREMANIAN, S., SVENSSON, K., TUMMERS, M. J. & MOSHFEGH, B. 2014 Near-field mixing of jets issuing from an array of round nozzles. *Int. J. Heat Fluid Flow* **47**, 84–100.

GOTTLIEB, S. & SHU, C.-W. 1998 Total variation diminishing Runge-Kutta schemes. *Math. Comp.* **67** (221), 73–85.

GAD-EL HAK, M. & CORRSIN, S. 1974 Measurements of the nearly isotropic turbulence behind a uniform jet grid. *J. Fluid Mech.* **62** (1), 115–143.

HAO, K., TIAN, A. & ZHOU, Y. 2021 Characteristics of small-scale motions in a dual-plane jet flow. *Int. J. Heat Fluid Flow* **91**, 108851.

HAYASHI, M., WATANABE, T. & NAGATA, K. 2021*a* Characteristics of small-scale shear layers in a temporally evolving turbulent planar jet. *J. Fluid Mech.* **920**, A38.

HAYASHI, M., WATANABE, T. & NAGATA, K. 2021*b* The relation between shearing motions and the turbulent/non-turbulent interface in a turbulent planar jet. *Phys. Fluids* **33** (5), 055126.

HWANG, W. & EATON, J. K. 2004 Creating homogeneous and isotropic turbulence without a mean flow. *Exp. Fluids* **36**, 444–454.

ISAZA, J. C., SALAZAR, R. & WARHAFT, Z. 2014 On grid-generated turbulence in the near-and far field regions. *J. Fluid Mech.* **753**, 402–426.

ISHIDA, T., DAVIDSON, P. A. & KANEDA, Y. 2006 On the decay of isotropic turbulence. *J. Fluid Mech.* **564**, 455–475.

JIANG, G.-S. & SHU, C.-W. 1996 Efficient implementation of weighted ENO schemes. *J. Comput. Phys.* **126** (1), 202–228.

KERR, R. M. 1985 Higher-order derivative correlations and the alignment of small-scale structures in isotropic numerical turbulence. *J. Fluid Mech.* **153**, 31–58.

KITAMURA, T., NAGATA, K., SAKAI, Y., SASOH, A. & ITO, Y. 2017 Changes in divergence-free grid turbulence interacting with a weak spherical shock wave. *Phys. Fluids* **29** (6).

Kitamura, T., Nagata, K., Sakai, Y., Sasoh, A., Terashima, O., Saito, H. & Harasaki, T. 2014 On invariants in grid turbulence at moderate Reynolds numbers. *J. Fluid Mech.* **738**, 378–406.

Kolmogorov, A. N. 1941 On decay of isotropic turbulence in an incompressible viscous liquid. In *Dokl. Akad. Nauk SSSR*, , vol. 31, pp. 538–540.

Kozul, M., Chung, D. & Monty, J. P. 2016 Direct numerical simulation of the incompressible temporally developing turbulent boundary layer. *J. Fluid Mech.* **796**, 437–472.

Krogstad, P.-Å. & Davidson, P. A. 2010 Is grid turbulence Saffman turbulence? *J. Fluid Mech.* **642**, 373–394.

Krogstad, P.-Å. & Davidson, P. A. 2011 Freely decaying, homogeneous turbulence generated by multi-scale grids. *J. Fluid Mech.* **680**, 417–434.

Kuo, A. Y.-S. & Corrsin, S. 1971 Experiments on internal intermittency and fine-structure distribution functions in fully turbulent fluid. *J. Fluid Mech.* **50** (2), 285–319.

Li, X.-L., Fu, D.-X., Ma, Y.-W. & Liang, X. 2010 Direct numerical simulation of compressible turbulent flows. *Acta Mech. Sin.* **26** (6), 795–806.

Lin, Y. F. & Sheu, M. J. 1990 Investigation of two plane paralleltiinven ilated jets. *Exp. Fluids* **10** (1), 17–22.

Liu, P., Duan, H. & Zhao, W. 2009 Numerical investigation of hot air recirculation of air-cooled condensers at a large power plant. *Appl. Therm. Eng.* **29** (10), 1927–1934.

Manohar, C. H. I., Sundararajan, T., Ramjee, V. & Kumar, S. S. 2004 A numerical and experimental investigation of the interactions between a non-uniform planar array of incompressible free jets. *Int. J. Numer. Methods Fluids* **44** (4), 431–446.

Medaouar, W., Loukarfi, L., Braikia, M., Khelil, A. & Naji, H. 2019 Experimental and numerical study of a turbulent multiple jets issued from lobed diffusers. *J. Appl. Fluid Mech.* **12** (3), 729–742.

Meldi, M. & Sagaut, P. 2013 Further insights into self-similarity and self-preservation in freely decaying isotropic turbulence. *J. Turbulence* **14** (8), 24–53.

Meslem, A., Nastase, I. & Allard, F. 2010 Passive mixing control for innovative air diffusion terminal devices for buildings. *Build. Environ.* **45** (12), 2679–2688.

Mi, J., Xu, M. & Zhou, T. 2013 Reynolds number influence on statistical behaviors of turbulence in a circular free jet. *Physics of Fluids* **25** (7), 075101.

Miller, D. R. & Comings, E. W. 1960 Force-momentum fields in a dual-jet flow. *J. Fluid Mech.* **7** (2), 237–256.

Mora, D. O, Muñiz Pladellorens, E., Riera Turró, P., Lagauzere, M. & Obligado, M. 2019 Energy cascades in active-grid-generated turbulent flows. *Phys. Rev. Fluids* **4** (10), 104601.

Mori, T., Watanabe, T. & Nagata, K. 2024 Nearly homogeneous and isotropic turbulence generated by the interaction of supersonic jets. *Exp. Fluids* **65** (4), 47.

Morize, C. & Moisy, F. 2006 Energy decay of rotating turbulence with confinement effects. *Phys. Fluids* **18** (6).

Mydlarski, L. & Warhaft, Z. 1996 On the onset of high-Reynolds-number grid-generated wind tunnel turbulence. *J. Fluid Mech.* **320** (1), 331–368.

Nagata, R., Watanabe, T. & Nagata, K. 2018 Turbulent/non-turbulent interfaces in temporally evolving compressible planar jets. *Phys. Fluids* **30** (10).

Pantano, C. & Sarkar, S. 2002 A study of compressibility effects in the high-speed turbulent shear layer using direct simulation. *J. Fluid Mech.* **451**, 329–371.

Pérez-Alvarado, A., Mydlarski, L. & Gaskin, S. 2016 Effect of the driving algorithm on the turbulence generated by a random jet array. *Exp. Fluids* **57**, 1–15.

Pineau, P. & Bogey, C. 2020 Temperature effects on convection speed and steepened waves of temporally developing supersonic jets. *AIAA J.* **58** (3), 1227–1239.

Praud, O., Fincham, A. M. & Sommeria, J. 2005 Decaying grid turbulence in a strongly stratified fluid. *J. Fluid Mech.* **522**, 1–33.

Raman, G. & Taghavi, R. 1996 Resonant interaction of a linear array of supersonic rectangular jets: an experimental study. *J. Fluid Mech.* **309**, 93–111.

van Reeuwijk, M. & Holzner, M. 2014 The turbulence boundary of a temporal jet. *J. Fluid Mech.* **739**, 254–275.

Sadeghi, H., Oberlack, M. & Gauding, M. 2018 On new scaling laws in a temporally evolving turbulent plane jet using Lie symmetry analysis and direct numerical simulation. *J Fluid Mech.* **854**, 233–260.

Saffman, P. G. 1967 The large-scale structure of homogeneous turbulence. *J. Fluid Mech.* **27**, 581–593.

Samtaney, R., Pullin, D. I. & Kosović, B. 2001 Direct numerical simulation of decaying compressible turbulence and shocklet statistics. *Phys. Fluids* **13** (5), 1415–1430.

San, O. & Kara, K. 2015 Evaluation of Riemann flux solvers for WENO reconstruction schemes: Kelvin–Helmholtz instability. *Comput. Fluids* **117**, 24–41.

da Silva, C. B. & Pereira, J. C. F. 2008 Invariants of the velocity-gradient, rate-of-strain, and rate-of-rotation tensors across the turbulent/nonturbulent interface in jets. *Phys. Fluids* **20** (5), 055101.

Sinhuber, M., Bodenschatz, E. & Bewley, G. P. 2015 Decay of turbulence at high Reynolds numbers. *Phys. Rev. Lett.* **114**, 034501.

Skrbek, L. & Stalp, S. R. 2000 On the decay of homogeneous isotropic turbulence. *Phys. Fluids* **12** (8), 1997–2019.

Sreenivasan, K. R. & Antonia, R. A. 1997 The phenomenology of small-scale turbulence. *Annu. Rev. Fluid Mech.* **29** (1), 435–472.

Svensson, K., Rohdin, P. & Moshfegh, B. 2016 On the influence of array size and jet spacing on jet interactions and confluence in round jet arrays. *J. Fluids Eng.* **138** (8), 081206.

Takahashi, M., Fukui, R., Tsujimoto, K., Ando, T. & Shakouchi, T. 2023 Helical structures in a temporally developing round jet in the developed state. *Flow, Turbul. Combust.* **111** (1), 59–79.

Tan, S., Xu, X., Qi, Y. & Ni, R. 2023 Scalings and decay of homogeneous, nearly isotropic turbulence behind a jet array. *Phys. Rev. Fluids* **8** (2), 024603.

Tanaka, K., Watanabe, T., Nagata, K., Sasoh, A., Sakai, Y. & Hayase, T. 2018 Amplification and attenuation of shock wave strength caused by homogeneous isotropic turbulence. *Phys. Fluids* **30** (3).

Tatsumi, K., Tanaka, M., Woodfield, P. L. & Nakabe, K. 2010 Swirl and buoyancy effects on mixing performance of baffle-plate-type miniature confined multijet. *Int. J. Heat Fluid Flow* **31** (1), 45–56.

Teunissen, H. W. 1975 Simulation of the planetary boundary layer in a multiple-jet wind tunnel. *Atmos. Environ.* **9** (2), 145–174.

Thielen, L., Jonker, H. J. J. & Hanjalić, K. 2003 Symmetry breaking of flow and heat transfer in multiple impinging jets. *Int. J. Heat Fluid Flow* **24** (4), 444–453.

Valente, P. C., da Silva, C. B. & Pinho, F. T. 2016 Energy spectra in elasto-inertial turbulence. *Phys. Fluids* **28** (7), 075108.

Valente, P. C. & Vassilicos, J. C. 2014 The non-equilibrium region of grid-generated decaying turbulence. *J. Fluid Mech.* **744**, 5–37.

Van Atta, C. W. & Antonia, R. A. 1980 Reynolds number dependence of skewness and flatness factors of turbulent velocity derivatives. *Phys. Fluids* **23** (2), 252–257.

Variano, E. A., Bodenschatz, E. & Cowen, E. A. 2004 A random synthetic jet array driven turbulence tank. *Exp. Fluids* **37**, 613–615.

Wang, J., Gotoh, T. & Watanabe, T. 2017 Shocklet statistics in compressible isotropic turbulence. *Phys. Rev. Fluids* **2** (2), 023401.

Watanabe, T., Mori, T., Ishizawa, K. & Nagata, K. 2024 Scale dependence of local shearing motion in decaying turbulence generated by multiple-jet interaction. *J. Fluid Mech.* **997**, A14.

Watanabe, T. & Nagata, K. 2018 Integral invariants and decay of temporally developing grid turbulence. *Phys. Fluids* **30** (10), 105111.

Watanabe, T., Riley, J. J., de Bruyn Kops, S. M., Diamessis, P. J. & Zhou, Q. 2016*a* Turbulent/non-turbulent interfaces in wakes in stably stratified fluids. *J. Fluid Mech.* **797**, R1.

Watanabe, T., Sakai, Y., Nagata, K., Ito, Y. & Hayase, T. 2014 Enstrophy and passive scalar transport near the turbulent/non-turbulent interface in a turbulent planar jet flow. *Phys. Fluids* **26** (10), 105103.

Watanabe, T., da Silva, C. B., Sakai, Y., Nagata, K. & Hayase, T. 2016*b* Lagrangian properties of the entrainment across turbulent/non-turbulent interface layers. *Phys. Fluids* **28** (3), 031701.

Watanabe, T., Tanaka, K. & Nagata, K. 2021 Solenoidal linear forcing for compressible, statistically steady, homogeneous isotropic turbulence with reduced turbulent mach number oscillation. *Phys. Fluids* **33** (9), 095108.

Watanabe, T., Zhang, X. & Nagata, K. 2018 Turbulent/non-turbulent interfaces detected in DNS of incompressible turbulent boundary layers. *Phys. Fluids* **30** (3), 035102.

Watanabe, T., Zhang, X. & Nagata, K. 2019 Direct numerical simulation of incompressible turbulent boundary layers and planar jets at high Reynolds numbers initialized with implicit large eddy simulation. *Comput. Fluids* **194**, 104314.

Watanabe, T., Zheng, Y. & Nagata, K. 2022 The decay of stably stratified grid turbulence in a viscosity-affected stratified flow regime. *J. Fluid Mech.* **946**, A29.

Xinliang, L., Dexun, F. & Yanwen, M. 2002 Direct numerical simulation of compressible isotropic turbulence. *Sci. China A.* **45**, 1452–1460.

Yamamoto, K., Ishida, T., Watanabe, T. & Nagata, K. 2022*a* Experimental and numerical investigation of compressibility effects on velocity derivative flatness in turbulence. *Phys. Fluids* **34** (5), 055101.

Yamamoto, K., Watanabe, T. & Nagata, K. 2022*b* Turbulence generated by an array of opposed piston-driven synthetic jet actuators. *Exp. Fluids* **63** (1), 35.

Yang, H., Wu, Y., Zeng, X., Wang, X. & Zhao, D. 2021 Partially-premixed combustion characteristics and thermal performance of micro jet array burners with different nozzle spacings. *J. Thermal Sci.* **30**, 1718–1730.

Yimer, J., Becker, H. A. & Grandmaison, E. W. 1996 Development of flow from multiple-jet burners. *Can. J. Chem. Eng.* **74** (6), 840–851.

Zecchetto, M. & da Silva, C. B. 2021 Universality of small-scale motions within the turbulent/non-turbulent interface layer. *J. Fluid Mech.* **916**, A9.

Zhang, X., Watanabe, T. & Nagata, K. 2018 Turbulent/nonturbulent interfaces in high-resolution direct numerical simulation of temporally evolving compressible turbulent boundary layers. *Phys. Rev. Fluids* **3** (9), 094605.

Zheng, Y., Nagata, K. & Watanabe, T. 2021 Energy dissipation and enstrophy production/destruction at very low Reynolds numbers in the final stage of the transition period of decay in grid turbulence. *Phys. Fluids* **33** (3).